

Magnetic mechanism for the biological functioning of hemoglobin

Selma Mayda,^{1,2} Zafer Kandemir,¹ Nejat Bulut,^{1,*} and Sadamichi Maekawa^{3,4}

¹*Department of Physics, Izmir Institute of Technology, Urla 35430, Turkey*

²*Department of Materials Science and Engineering,
Izmir Institute of Technology, Urla 35430, Turkey*

³*RIKEN Center for Emergent Matter Science, Wako 351-0198, Japan*

⁴*Kavli Institute for Theoretical Sciences,
University of Chinese Academy of Sciences, Beijing 100049, China*

(Dated: January 13, 2022)

Abstract

The role of magnetism in the biological functioning of hemoglobin has been debated since its discovery by Pauling and Coryell in 1936. The hemoglobin molecule contains four heme groups each having a porphyrin layer with a Fe ion at the center. Here, we present combined density-functional theory and quantum Monte Carlo calculations for an effective model of Fe in a heme cluster. In comparison with these calculations, we analyze the experimental data on human adult hemoglobin (HbA) from the magnetic susceptibility, Mössbauer and magnetic circular dichroism (MCD) measurements. In both the deoxygenated (deoxy) and the oxygenated (oxy) cases, we show that local magnetic moments develop in the porphyrin layer with antiferromagnetic coupling to the Fe moment. Our calculations reproduce the magnetic susceptibility measurements on deoxy and oxy-HbA. For deoxy-HbA, we show that the anomalous MCD signal in the UV region is an experimental evidence for the presence of antiferromagnetic Fe-porphyrin correlations. The various important properties of hemoglobin are explained based on the antiferromagnetic correlations including the Bohr effect and cooperativity. This analysis shows that magnetism is involved in a fundamental way in the functioning of hemoglobin.

Pauling and Coryell showed that the magnetic susceptibility of deoxy-HbA exhibits a Curie-type ($1/T$) temperature dependence, while for oxy-HbA it is weakly negative implying that the total spin $S = 0$ for the molecule^{1,2}. Mössbauer experiments³ are consistent with the view that Fe is in an $S = 2$ state in deoxy-HbA, while its magnetic moment is found to be $\lesssim 1 \mu_B$ in the oxy case. The magnetic circular dichroism (MCD) measurements⁴ find an anomalous line shape for the temperature-dependent MCD spectra in the UV region. The HbA molecule exhibits remarkable functional properties such as the cooperativity⁵⁻⁷ and the Bohr effect⁸⁻¹¹, which enhance its oxygen carrying capacity. When one of the four Fe ions in HbA combines an oxygen molecule, the other three Fe ions attract oxygens cooperatively. The Bohr effect denotes the characteristic of HbA through which the oxygen affinity depends on the pH of the medium. There is currently no broad agreement on the spin and charge distributions and the role of magnetism in HbA¹²⁻¹⁷.

We study the electronic state of one heme group by using an effective multi-orbital Anderson impurity model^{18,19}. The parameters of this model are obtained by the density functional theory²⁰ (DFT) calculations, where we use the molecular coordinates determined by the X-ray measurements^{21,22}. This way the stereochemical effects are included. We then study this model with the quantum Monte Carlo (QMC) simulations²³. This DFT+QMC approach is described in the Methods section.

Figure 1(a) shows the molecular structure of deoxy-HbA²². We have performed our DFT+QMC calculations for the truncated clusters shown in Figs. 1(b) and (c).

Figure 2 shows DFT+QMC results for the magnetic-moment density $M(\mathbf{r})$ at temperature $T = 150$ K. In the deoxy case, we observe that the Fe site has a large up moment $\approx 4.6 \mu_B$. The neighboring nitrogen sites have smaller moments, while at the carbon sites $M(\mathbf{r})$ points down. These down moments originate from the partially-occupied π^* host states consisting of the $C(2p_z)$ orbitals. Hence, antiferromagnetic correlations exist between the large Fe magnetic moment and the host moments spread out in the porphyrin layer in deoxy-heme. In oxy-heme, the Fe moment is reduced, but remains finite. In addition, the neighboring O_2 and N sites have magnetic moments which are antiferromagnetically coupled to that of Fe. In the oxy case, the antiferromagnetic screening cloud is more tightly localized around the Fe site. The calculation of $M(\mathbf{r})$ is described in the Supplementary Information. Additional DFT+QMC data on the spin and charge distributions are presented in the Methods section.

Figure 3(a) shows the temperature dependence of the total spin susceptibility χ_t . For the deoxy-heme cluster, χ_t follows a nearly-perfect Curie T -dependence. The total effective magnetic mo-

ment M_t is $\approx 4.1 \mu_B$ at $T = 150$ K, which is reduced from that of Fe due to the Fe-porphyrin antiferromagnetic correlations. In the oxy case, there are two temperature regimes separated by a crossover temperature $T^* \approx 300$ K: In the high- T regime, $T > T^*$, χ_t has a Curie-type T dependence with an effective total moment $\approx 2.1 \mu_B$. In the low- T regime, $T < T^*$, χ_t decreases rapidly as T decreases. For $T > 300$ K, the reduction of χ_t with respect to that of deoxy-heme is mainly due to the collapse of the Fe magnetic moment because of the loss of the ferromagnetic correlations among the Fe($3d_v$) orbitals. For $T < 300$ K, $\chi_t \rightarrow 0$ with the opening of a magnetic gap at the Fermi level. This is clearly seen in Fig. 3(b), which shows that the total moment M_t gets suppressed within $\Delta_S \approx 0.15$ eV of the Fermi level as T decreases. This gap arises from the transfer of electrons from mainly the O_2 to the Fe($3d_v$) orbitals, in particular, to the so-called t_{2g} orbitals, $v = xy, xz$ and yz . These are discussed further in the Methods section.

Experimentally, the spin susceptibility of oxy-HbA vanishes at room temperature^{1,24}, while we find that $\chi_t \approx 150 \mu_B^2/\text{eV}$ per heme. It is possible that because of the various approximations introduced, the DFT+QMC approach is underestimating the value of T^* . If this is indeed the case, then it will have important consequences for the binding mechanism of O_2 to Fe in heme and the Bohr effect: We note that, in general, charge transfer to the Fe($3d$) orbitals would be energetically costly because of the large Coulomb repulsion over there. However, as seen in the Methods section, in heme this is overcome by making use of the the upper-Hubbard level of the Fe($3d_{xy}$) orbital. This is where the Fe($3d_{xy}$) orbital becomes doubly occupied, and it is located very close to the Fermi level. This turns out to be an important feature of the electronic structure of oxy-heme, because when the chemical potential is away from this region, the magnetic gap does not open. We think that, in order to minimize its energy, the system is developing magnetic moments and magnetic correlations by redistributing electrons. It is a real possibility that the gain in energy by going to the $S = 0$ state is responsible for the binding of O_2 to heme. These suggest that the binding of O_2 to Fe in heme has a magnetic origin. We note that the stereochemical effects⁶ are clearly important in O_2 binding. We are proposing that the magnetism, which is controlled by the stereochemical effects, has the key role in the perfectly reversible binding of O_2 to Fe in heme.

In the Bohr effect, the oxygen affinity of HbA is controlled by the hydrogen ion concentration in the red blood cells. We have seen above that the $S = 0$ state is developing within a narrow energy window at the Fermi level. Hence, the magnetic properties depend sensitively on the electron filling. Any changes which effectively moves the chemical potential away from this narrow region will affect the binding of O_2 . This could be how the pH influences the oxygen affinity.

We note that the above suggested mechanism for the Fe-oxygen bonding may not be limited to heme, but may also be relevant for bonding in other compounds containing transition metals, for example the transition-metal oxides. This type of bonding is more complicated than the usual covalent or ionic bondings because it involves the upper-Hubbard level of the $3d$ orbitals and the magnetic correlations.

An important feature which emerges from these calculations is the antiferromagnetic coupling between Fe and the porphyrin layer. Experimental evidence for this is provided by the MCD data on deoxy-HbA in the UV region. The MCD intensity $\Delta\varepsilon(E)$ is the difference between the left-circularly polarized (LCP) and the right-circularly polarized (RCP) light absorption within an applied magnetic field parallel to the direction of light propagation. The MCD spectrum of deoxy-HbA has a peak in the UV region at ≈ 3 eV which has an anomalous line shape and a $1/T$ temperature-dependence⁴. The optical absorption $\varepsilon(E)$ has a T -independent peak at the same energy. It is known that the optical absorption at ≈ 3 eV is due to $\pi \rightarrow \pi^*$ transitions between the bonding π and antibonding π^* states⁴. The MCD spectrum of deoxy-HbA in UV region is anomalous in the following sense: In the usual case, the T -dependent piece of the MCD spectrum first has a dip and then a peak as the frequency increases, whereas in deoxy-HbA the MCD spectrum first has a peak and then a shallow dip. Here, we propose that the anomalous MCD signal is caused by the orbital-selective optical transitions from the occupied π orbitals to two partially occupied π^* orbitals, which we label as π_1^* and π_2^* . According to the DFT+QMC calculations, the π_1^* state is nearly half-filled while the π_2^* is nearly empty, which is discussed further in the Methods section.

As illustrated in Fig. 4(a), within an applied field \mathbf{B}_{app} pointing up, the Fe spin will be polarized in the down direction. Meanwhile, the spin polarization of π_1^* will be parallel to the field, because of the Fe- π_1^* antiferromagnetic correlations. Hence, during an LCP (RCP) optical transition from the π state, it will be energetically more favorable for the π_1^* (π_2^*) state to absorb a down-spin (up-spin) electron. These orbital-selective optical transitions are illustrated in Figs. 4(b) and (c). We have calculated the MCD spectrum due to these transitions as discussed in the Methods section. Figures 4(d) and (e) present the experimental and the calculated MCD spectra, respectively. The inset of Fig. 4(d) illustrates the line shape normally expected for the T -dependent MCD spectrum²⁵. The anomalous MCD line shape of deoxy-HbA seen in Fig. 4(d) had been attributed to a negative spin-orbit coupling⁴. We are suggesting that it instead originates from the antiferromagnetic coupling between the Fe($3d$) and π^* states. Because of this, π_1^* and π_2^* porphyrin states act as if they have negative g -factors. The agreement with the experimental data can be improved

further by incorporating into the analysis the optical absorption data as shown in the Methods section.

Discussion of cooperativity requires a multi-heme model. However, because of its importance, we will briefly comment on the implications of the DFT+QMC results. Assuming independent heme groups, the magnetic susceptibility measurements yield an effective magnetic moment per heme $M_{\text{heme}} = 5.46 \mu_{\text{B}}$ in deoxy-HbA¹. Since this is larger than the spin $S = 2$ value of $4.9 \mu_{\text{B}}$, Pauling and Coryell already pointed out the possibility of inter-heme ferromagnetic correlations¹. The DFT+QMC calculations find $M_{\text{heme}} \approx 4.1 \mu_{\text{B}}$. This requires an average inter-heme magnetic correlation $\langle M_{\text{heme},1}^z M_{\text{heme},2}^z \rangle \approx 4.3 \mu_{\text{B}}^2$ for deoxy-HbA, which is significant. We note that sufficiently strong inter-heme magnetic correlations could lead to cooperativity: The first O₂ to bind Fe needs to overcome the inter-heme ferromagnetic interaction. Upon O₂ binding to Fe, the magnetic moment of that heme group vanishes. The following O₂'s will bind more easily because of the loss of the inter-heme ferromagnetic correlations. An alternative scenario is based on the spin non-conservancy in the binding of O₂ to heme. We note that while O₂ is in a triplet state ($S = 1$) and deoxy-heme is considered to be $S = 2$, the resultant oxy-heme is in an $S = 0$ state. This non-conservancy of the total spin in the binding of O₂ may be limiting the reaction rate. However, because of inter-heme ferromagnetic correlations, spin transfer may be possible among the heme groups. Hence, when the O₂'s bind cooperatively, the spin can be conserved, thus eliminating the limit on the O₂ binding rate.

We have shown that magnetic moments and magnetic correlations exist in deoxy and oxy-HbA. In addition, the charge transfer from oxygen to Fe and the magnetic gap are key electronic properties of oxy-HbA. It is remarkable that evolution has been able to utilize these properties, which arise from the strongly-correlated electrons, for the functioning of hemoglobin. We note that there are a large number of metalloproteins, metalloenzymes and other bioinorganic molecules containing transition-metal centers²⁶. Hence, the magnetic effects are poised to have a general role in the functioning of bioinorganic molecules with a distinct place in the emerging field of quantum biology.

* nejatbulut@iyte.edu.tr

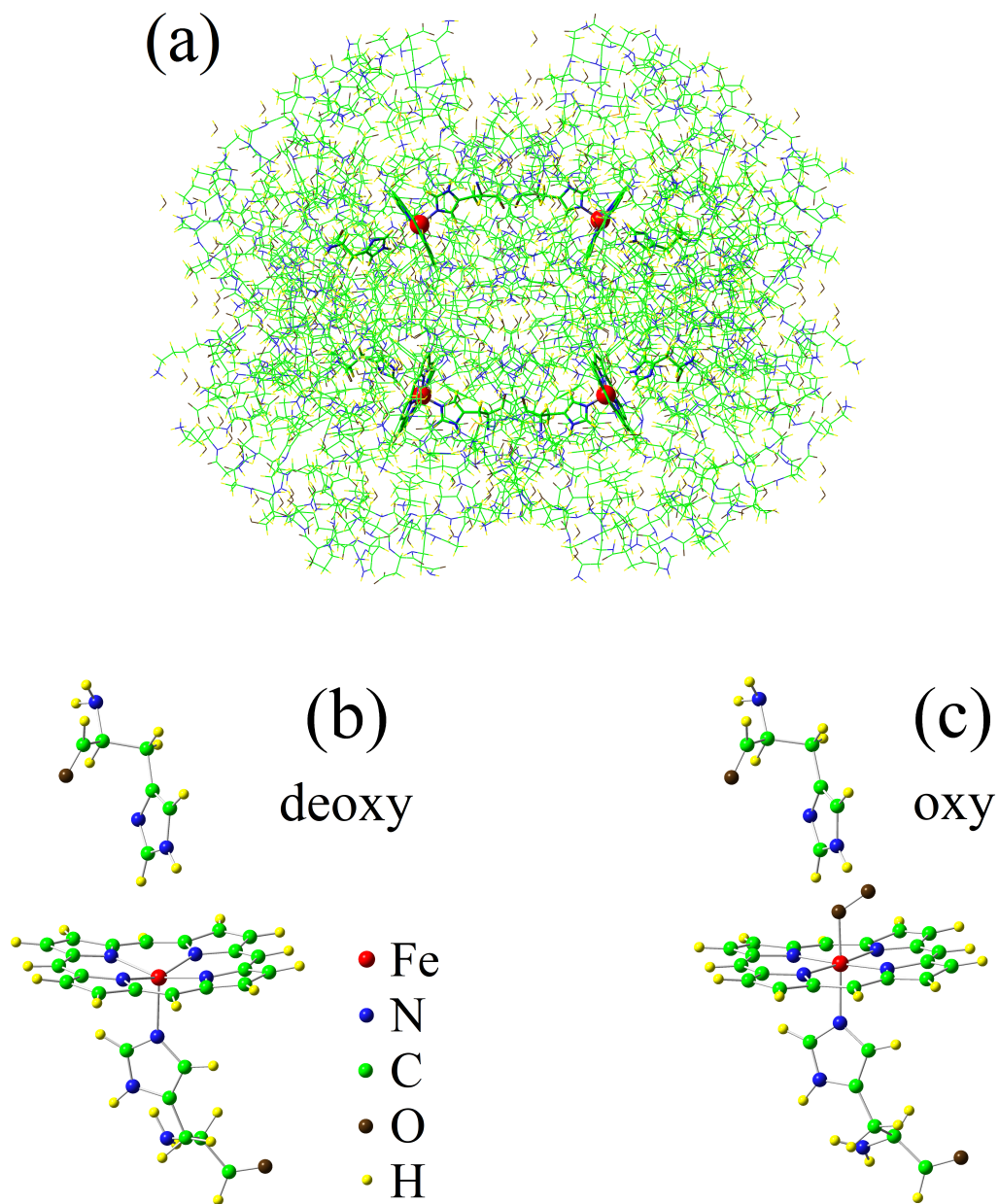
¹ Pauling, L. & Coryell, C. D. The magnetic properties and structure of hemoglobin, oxyhemoglobin and

- carbonmonoxyhemoglobin. *Proc. Natl. Acad. Sci. USA* **22**, 210 (1936).
- ² Bren, K. L., Eisenberg, R. & Gray, H. B. Discovery of the magnetic behavior of hemoglobin: A beginning of bioinorganic chemistry. *Proc. Natl. Acad. Sci. USA* **112**, 13123 (2015).
 - ³ Lang, G. & Marshall, W. Mössbauer effect in some hemoglobin compounds. *Proc. Phys. Soc.* **87**, 3 (1966).
 - ⁴ Treu, J. I. & Hopfield, J. J. Magnetic circular dichroism in hemoglobin. *J. Chem. Phys.* **63**, 613 (1975).
 - ⁵ Monod, J., Wyman, J. & Changeux, J. P. On the nature of allosteric transitions: a plausible model. *J. Mol. Biol.* **12**, 88 (1965).
 - ⁶ Perutz, M. F. Stereochemistry of cooperative effects in hemoglobin. *Nature* **228**, 726 (1970).
 - ⁷ Yuan, Y., Tam, M. F., Simplaceanu, V. & Ho, C. New look at hemoglobin allostery. *Chem. Rev.* **115**, 1702 (2015).
 - ⁸ Adair, G. S. The osmotic pressure of haemoglobin in the absence of salts. *Proc. R. Soc. Lond. A* **109**, 292 (1925).
 - ⁹ Adair, G. S. The hemoglobin system VI. The oxygen dissociation curve of hemoglobin, *J. Bio. Chem.* **63**, 529 (1925).
 - ¹⁰ Ferry, R. M. & Green, A. A. Studies in the chemistry of hemoglobin III. The equilibrium between oxygen and hemoglobin and its relation to changing hydrogen ion activity. *J. Bio. Chem.* **81**, 175 (1929).
 - ¹¹ Pauling, L. The oxygen equilibrium of hemoglobin and its structural interpretation. *Proc. Natl. Acad. Sci.* **21**, 186 (1935).
 - ¹² Weiss, J. J. Nature of the iron-oxygen bond in oxyhemoglobin. *Nature* **202**, 83 (1964).
 - ¹³ Pauling, L. Nature of the iron-oxygen bond in oxyhemoglobin. *Nature* **203**, 182 (1964).
 - ¹⁴ McClure, D. S. Electronic structure of transition-metal complex ions. *Radiation Res. Supp.* **2**, 218 (1960).
 - ¹⁵ Goddard, W. A, III & Olafson, B. D. Ozone model for bonding of an O₂ to heme in oxyhemoglobin. *Proc. Natl. Acad. Sci. USA* **72**, 2335 (1975).
 - ¹⁶ Scheidt, W. R. & Reed, C. A. Spin-state/stereochemical relationships in iron porphyrins: implications for the hemoproteins. *Chem. Rev.* **81**, 543 (1981).
 - ¹⁷ Chen, H., Ikeda-Saito, M. & Shaik, S. Nature of the Fe-O₂ bonding in oxy-myoglobin: effect of the protein. *J. Am. Chem. Soc.* **130**, 14778 (2008).
 - ¹⁸ Anderson, P. W. Localized magnetic states in metals. *Phys. Rev.* **124**, 41 (1961).
 - ¹⁹ Haldane, F. D. M. & Anderson, P. W. Simple model of multiple charge states of transition-metal impu-

- rities in semiconductors. Phys. Rev. B **13**, 2553 (1976).
- ²⁰ Kohn, W. & Sham, L. J. Self-consistent equations including exchange and correlation effects. Phys. Rev. **140**, A1133 (1965).
- ²¹ Perutz, M. F. et al. Structure of hemoglobin: a three-dimensional Fourier synthesis at 5.5-Å resolution, obtained by X-ray analysis. Nature **185**, 416 (1960).
- ²² Park, S. Y., Yokoyama, T., Shibayama, N., Shiro, Y. & Tame, J. R. H. 1.25 Å Resolution crystal structures of human hemoglobin in the oxy, deoxy and carbonmonoxy forms. J. Mol. Biol **360**, 690 (2006).
- ²³ Hirsch, J. E. & Fye, R. M. Monte Carlo method for magnetic impurities in metals. Phys. Rev. Lett. **56**, 2521 (1986).
- ²⁴ Pauling, L. Magnetic properties and structure of oxyhemoglobin. Proc. Nat. Acad. Sci. USA, **74**, 2612 (1977).
- ²⁵ Mason, W. R. *A Practical Guide to Magnetic Circular Dichroism Spectroscopy*. John Wiley & Sons, Inc. (2007).
- ²⁶ Gray, H. B. Biological inorganic chemistry at the beginning of the 21st century. Proc. Natl. Acad. Sci. USA **100**, 3563 (2003).

Acknowledgements We thank Nuran Elmaci Irmak, Talat Yalcin, Acar Savaci and Tahir Cagin for comments. Support by the Turkish Scientific and Technical Research Council (TUBITAK grant number 113F242) is gratefully acknowledged. This work was supported by JST ERATO Grant No. JPMJER1402, JSPS Grant-in-Aid for Scientific Research on Innovative Areas Grant No. JP26103005, and JSPS KAKENHI Grant Nos. JP16H04023 and JP17H02927. The numerical calculations reported here were performed at the TUBITAK ULAKBIM High Performance and Grid Computing Center (TRUBA resources).

FIG. 1 | Molecular structure of HbA and the heme clusters



(a) Molecular structure of deoxy-HbA obtained by X-ray diffraction²² (Protein Data Bank, Keyword: 2DN2). Truncated (b) deoxy and (c) oxy-heme clusters which we have used in the DFT+QMC calculations. The way these clusters are obtained from the full HbA molecular structures is described in the Supplementary Information.

FIG. 2 | Magnetic-moment density

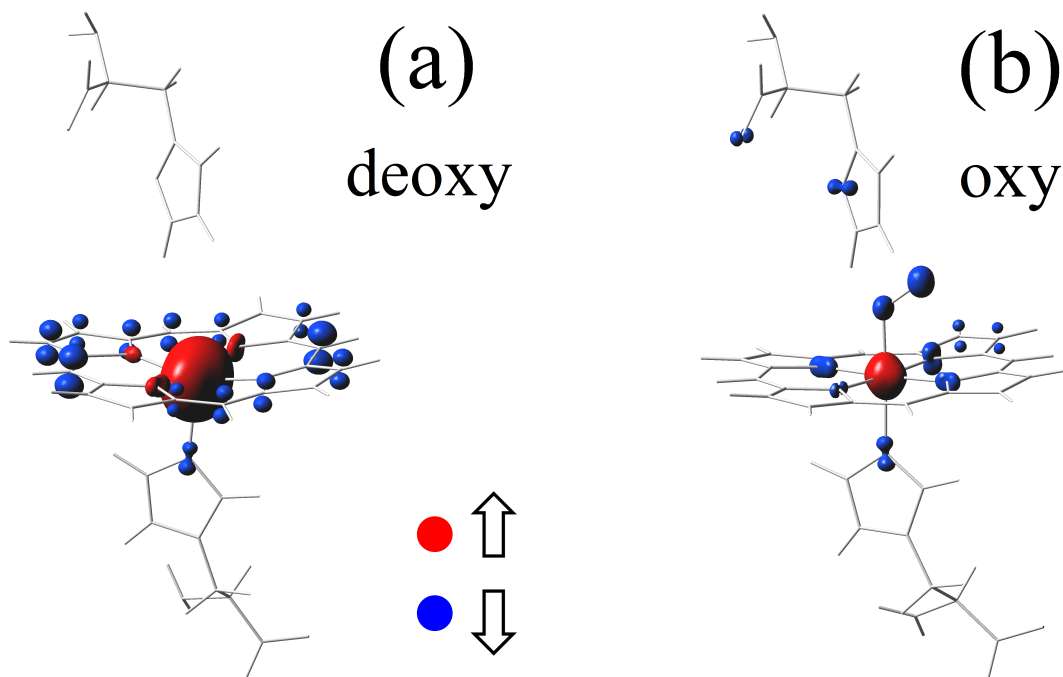
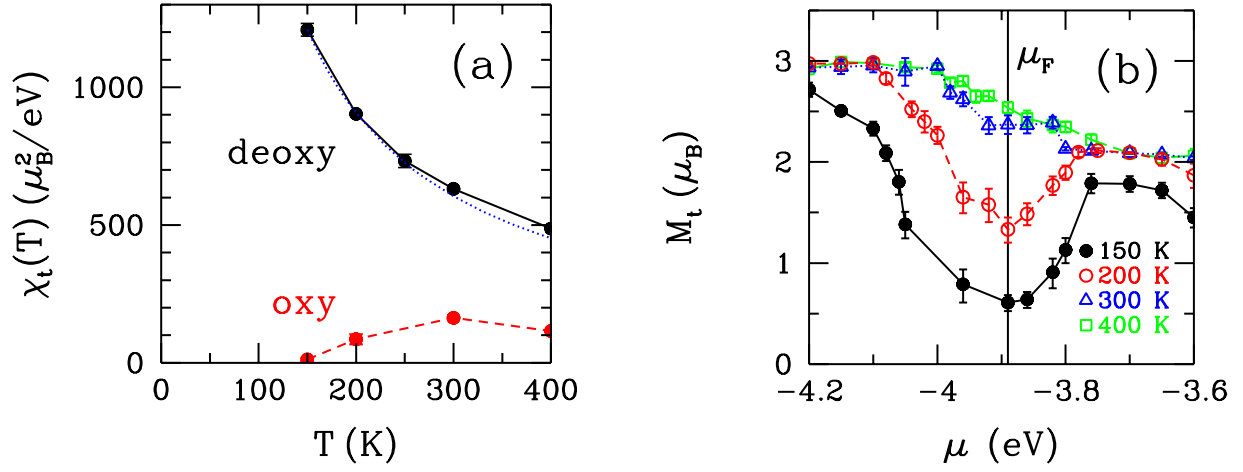


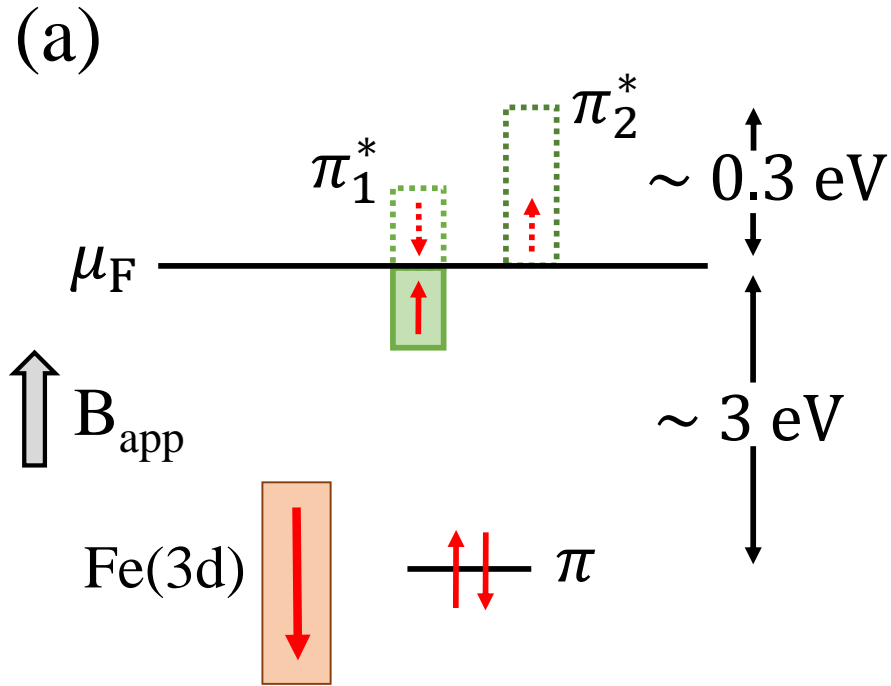
Illustration of the magnetic-moment density $M(\mathbf{r})$ for (a) the deoxy and (b) oxy-heme clusters at $T = 150$ K. Here, the red (blue) color indicates the atomic orbitals which have magnetic moments pointing up (down). The magnitude of $M(\mathbf{r})$ at an atomic site is proportional to the volume of the bubble at that site. The calculation of $M(\mathbf{r})$ is described in the Supplementary Information.

FIG. 3 | Spin susceptibility and the magnetic moment

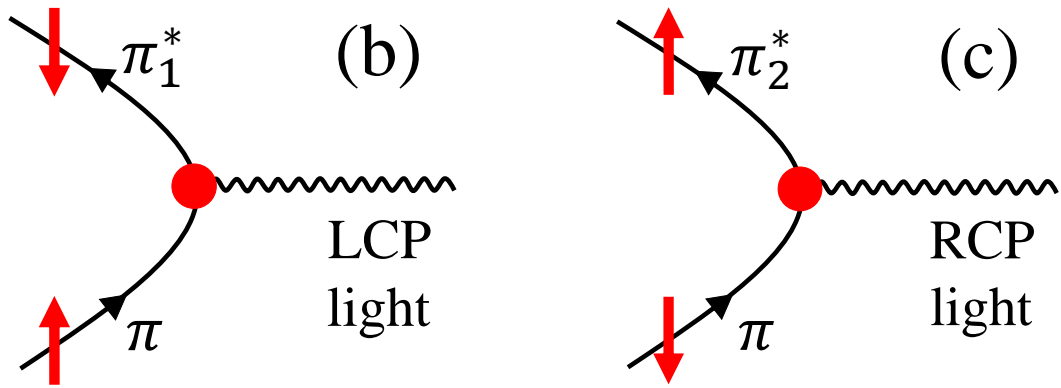


(a) Temperature dependence of the total spin susceptibility χ_t for the deoxy and oxy-heme clusters. The blue dotted curve denotes the Curie ($1/T$) temperature dependence. (b) Total magnetic moment M_t versus the chemical potential μ near the Fermi level μ_F at various temperatures for the oxy-heme cluster. Here, the black vertical line denotes μ_F at $T = 150$ K.

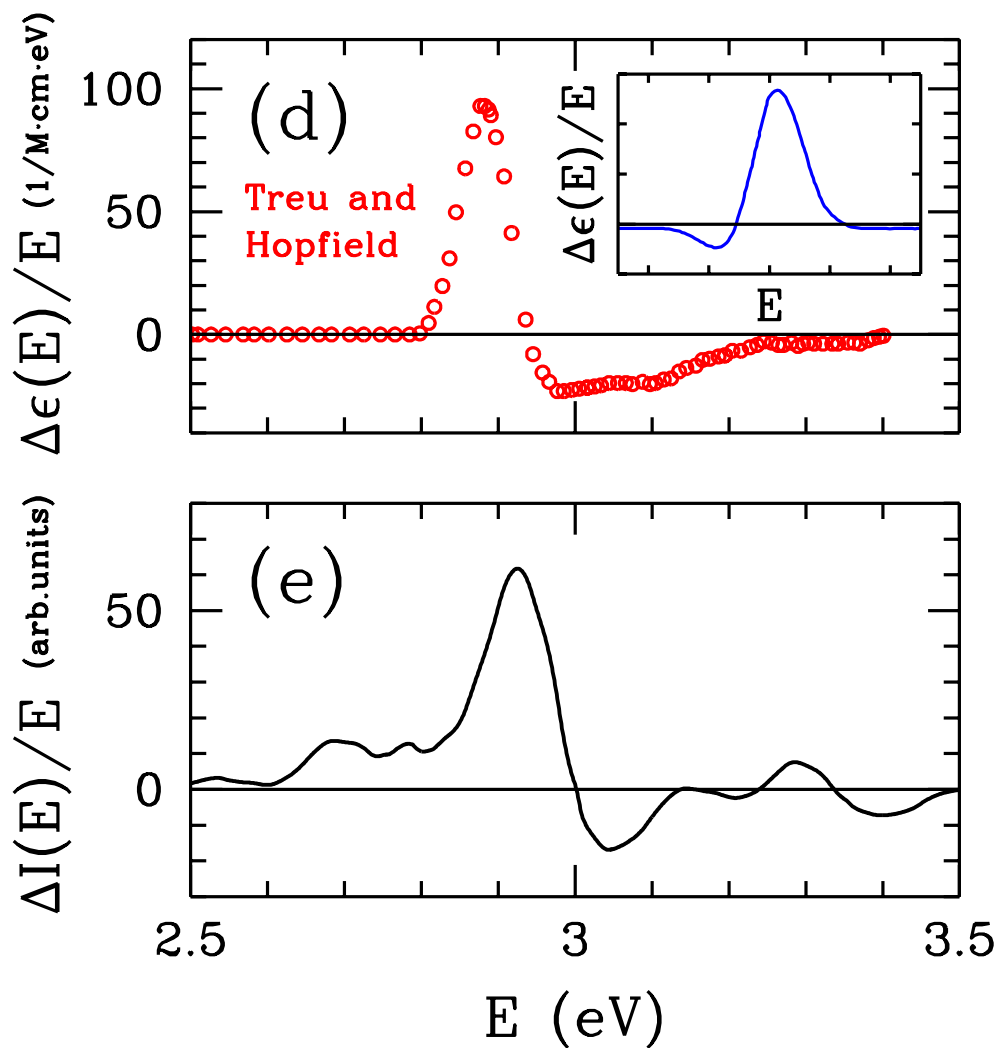
FIG. 4 | Anomalous MCD spectrum of deoxy-HbA in the UV region



(a) Illustration of the spin polarizations for the Fe(3d), and the bonding π and the antibonding π_1^* and π_2^* host states in an applied magnetic field \mathbf{B}_{app} for deoxy-heme. For \mathbf{B}_{app} pointing up, the total Fe(3d) spin gets polarized in the down direction, while the spin of the nearly half-filled π_1^* state gets polarized parallel to the field. The π_2^* state is nearly empty. From the DFT+QMC results we know that the π states are located about 3 eV below the Fermi level, and the widths of the π_1^* and π_2^* states are about 0.3 eV.



(b) Feynman diagram representing the absorption of LCP light in the optical transition $\pi \rightarrow \pi_1^*$. Here, an up-spin electron in a π state makes a transition to the π_1^* state becoming down-spin by absorbing LCP light (denoted by the wavy line). In (c), the $\pi \rightarrow \pi_2^*$ transition is shown for the absorption of RCP light, where a down-spin π electron makes a transition to the π_2^* state becoming up-spin. Here, the red dot is the effective vertex for the optical transition. Even though there is spin-orbit interaction only at the Fe(3d) orbitals, the π states can gain an effective spin-orbit coupling through antiferromagnetic coupling and hybridization with the Fe(3d) orbitals, which are discussed in the Methods section.



(d) Anomalous MCD line shape in the UV region for deoxy-HbA from the experiments by Treu and Hopfield⁴. Inset: Line shape normally expected for the temperature-dependent MCD spectrum²⁵. (e) Results from our calculation of the MCD spectrum for the deoxy-heme cluster.

METHODS

Effective Anderson impurity model for heme

We use an effective multi-orbital Anderson impurity model^{18,19}, where the five Fe(3d) orbitals are taken as the impurity states and the remaining orbitals are treated as the host states, to describe the electronic properties of the deoxy and oxy-heme clusters. The multi-orbital Anderson Hamiltonian with the intra and inter-orbital Coulomb interactions is given by

$$H = \sum_{m,\sigma} (\epsilon_m - \mu) c_{m\sigma}^\dagger c_{m\sigma} + \sum_{v,\sigma} (\epsilon_{dv} - \mu) d_{v\sigma}^\dagger d_{v\sigma} + \sum_{m,v,\sigma} (V_{mv} c_{m\sigma}^\dagger d_{v\sigma} + V_{mv}^* d_{v\sigma}^\dagger c_{m\sigma}) \quad (1)$$

$$+ \sum_v U n_{v\uparrow} n_{v\downarrow} + \sum_{v>v',\sigma} (U' n_{v\sigma} n_{v'-\sigma} + (U' - J) n_{v\sigma} n_{v'\sigma}),$$

where $c_{m\sigma}^\dagger$ ($c_{m\sigma}$) operator creates (annihilates) an electron in the m 'th host state with spin σ , $d_{v\sigma}^\dagger$ ($d_{v\sigma}$) is the creation (annihilation) operator for a localized electron with spin σ at the Fe(3d_v) orbital, and the electron occupation operator for the Fe(3d_v) orbitals is $n_{v\sigma} = d_{v\sigma}^\dagger d_{v\sigma}$. The energies of the host and the Fe(3d_v) states are ϵ_m and ϵ_{dv} , respectively. The hybridization matrix element between the m 'th host state and the Fe(3d_v) orbital is V_{mv} . The intra-orbital Coulomb repulsion is U , while U' and $U'' = U' - J$ are the Coulomb interactions between two 3d electrons in different orbitals with antiparallel and parallel spins, respectively. Here, J is the ferromagnetic Hund's coupling constant. In the case of a free atom, the relation $U' = U - 2J$ holds, which we also use here. The chemical potential μ is introduced because the QMC calculations are performed at finite temperatures in the grand canonical ensemble. At each value of the temperature, we adjust μ so that the cluster has the correct number of electrons, which is discussed below in Extended Data Fig. 3. We obtain the values of ϵ_m , ϵ_{dv} and V_{mv} by the density-functional theory (DFT)²⁰, which is discussed in the Supplementary Information. For the interaction parameters we use $U = 4$ eV and $J = 0.9$ eV.

We have performed the DFT+QMC calculations for clusters obtained by truncating the full deoxy and oxy-heme molecular structures from the Protein Data Bank as described in the Supplementary Information. For understanding the functioning of HbA, the role of the stereochemical effects have been investigated. In particular, it has been emphasized that Fe moves by about 0.4 Å towards the porphyrin ring upon O₂ binding²¹. Since we are using coordinates determined by the X-ray measurements, these stereochemical effects are already included in our model.

In Eq. (1), we include the longitudinal component of the Hund's interaction, however the transverse component, which consists of the spin-flip and the pair-hopping terms, is not included. In

addition, we neglect the temperature dependence of the molecular coordinates. In spite of these approximations, the DFT+QMC technique applied to this effective impurity model offers a realistic treatment for the electronic state of HbA. Comparisons with the experimental data on the magnetic properties show that we capture the connection between the magnetism and the biological functioning at least at a qualitative level. We note that these DFT+QMC calculations represent the only computational approach which yields agreement with the magnetic susceptibility, Mössbauer, and the MCD data on HbA at the same time.

Additional DFT+QMC data on the spin and charge distributions in the heme clusters

Extended Data Tables I(a) and (b) show the electron occupation number $\langle n_v \rangle$ and the effective magnetic moment M_v^{eff} of the Fe($3d_v$) orbitals (in units of Bohr magnetons μ_B) for the deoxy and oxy-heme clusters. Extended Data Table I(c) shows the total Fe($3d$) moment M_{3d} , the total host moment M_h , and the total moment M_t of the cluster. In addition, the Fe($3d$)-host magnetization correlation function $\langle M_{3d}^z M_h^z \rangle$ is shown (in μ_B^2). The values of the Fe($3d$), the host and the total effective spins denoted by S_{3d} , S_h and S , respectively, are also listed. The Monte Carlo statistical errors in $\langle n_v \rangle$ and M_v^{eff} are less than 2 percent. The QMC finite- $\Delta\tau$ effects on these are discussed below in Extended Data Fig. 4. In Extended Data Tables I(d)-(f), results on the magnetization correlation function $\langle M_v^z M_{v'}^z \rangle$ are shown (in μ_B^2) for the deoxy- and oxy-heme clusters at various temperatures. Here, the statistical errors are less than $0.04 \mu_B^2$. Extended Data Table I(g) compares the total intra and inter-orbital magnetic correlations among the Fe($3d$) orbitals for the deoxy and the oxy cases. In these quantities, the statistical errors are less than $0.1 \mu_B^2$.

For the deoxy case, we see that $\langle n_v \rangle$ is close to unity for all five of the $3d$ orbitals. The total number of the Fe($3d$) electrons $\langle n_{3d} \rangle = 5.38$ at $T = 300$ K, hence Fe is in between the ferric (+3) than the ferrous (+2) states. These orbitals are nearly fully polarized where the corresponding M_v^{eff} s are slightly less than $1 \mu_B$. The total effective moment of the $3d$ orbitals M_{3d} is $4.56 \mu_B$, while for the host $M_h = 1.06 \mu_B$. The total moment $M_t = 4.08 \mu_B$ is less than M_{3d} , because of the Fe($3d$)-host antiferromagnetic correlations. We find the effective Fe($3d$) spin S_{3d} to be 1.83, while the total spin $S = 1.60$. As T is lowered from 300 K to 150 K, these values for the electron occupations, effective moments and spins show almost no variation in the deoxy case.

In the oxy-heme case, the total Fe($3d$) electron number is 5.83 at 300 K. As T decreases to 150 K, $\langle n_{3d} \rangle$ increases to 6.07. This is due to charge transfer from mainly the O_2 to the Fe($3d$) orbitals. In the oxy case at 150 K, we have $\langle n_{xy} \rangle = 1.88$, hence this orbital is nearly doubly-occupied. The remaining orbitals are closer to half-filling.

At 300 K for the deoxy-heme $M_{3d} = 4.56 \mu_B$, while it is $2.50 \mu_B$ in the oxy case. Upon lowering T to 150 K, M_{3d} of oxy-heme decreases to $1.65 \mu_B$. This drop in M_{3d} is mainly due to the loss of the ferromagnetic correlations among the Fe($3d$) orbitals. This is seen by comparing the results on $\langle M_{\nu}^z M_{\nu'}^z \rangle$ shown in Extended Data Tables I(d)-(f) for the deoxy and oxy-heme clusters. We note that the total effective Fe($3d$) moment is obtained from

$$\langle (M_{3d}^z)^2 \rangle = \sum_{\nu} \langle (M_{\nu}^z)^2 \rangle + \sum_{\nu, \nu' \neq \nu} \langle M_{\nu}^z M_{\nu'}^z \rangle. \quad (2)$$

Extended Data Table I(g) compares the components of this expression for the deoxy and oxy cases, where we clearly see the loss of the inter-orbital ferromagnetic correlations and its effect on M_{3d} .

In Extended Data Fig. 1(a), we compare the total spin susceptibility of the cluster χ_t with the Fe($3d$) susceptibility χ_{Fe} . For the deoxy case, we see that χ_t is reduced with respect to χ_{Fe} due to the Fe-porphyrin antiferromagnetic coupling. Here, we also observe that χ_{Fe} obeys a perfect Curie T -dependence. In the oxy case, there is little difference between χ_t and χ_{Fe} . Both increase as $1/T$ for T down to 300 K. As T decreases below 300 K, a magnetic gap opens at the Fermi level which causes χ_{Fe} and χ_t to vanish.

In Extended Data Fig. 1(b), χ_t of the oxy-heme cluster is shown as a function of μ for various T . Here, we clearly observe the development of a spin gap with $2\Delta_S \approx 0.3$ eV at low T .

Additional DFT+QMC data on the O₂ to Fe charge transfer and the magnetic gap in oxy-heme

In Extended Data Fig. 2(a), we see that the total electron number in the Fe($3d$) orbitals $\langle n_{3d} \rangle$ develops a peak at the Fermi level $\mu_F \approx -3.9$ eV at low T . Extended Data Fig. 2(b) shows $\langle n_{\nu} \rangle$ versus μ for the five Fe($3d_{\nu}$) orbitals. We observe that, if μ is kept fixed at -3.9 eV as T is lowered from 400 K to 200 K, then $\langle n_{\nu} \rangle$ for the t_{2g} orbitals ($\nu = xy, xz,$ and yz) gets enhanced. In this case, the $3d_{xy}$ orbital has the largest increase. Meanwhile, for the e_g orbitals ($\nu = 3z^2 - r^2$ and $x^2 - y^2$) $\langle n_{\nu} \rangle$ gets suppressed. These show that the $3d$ orbitals are strongly coupled to each other as well as to their environment. We also observe that the upper Hubbard level of the $3d_{xy}$ orbital shifts down in energy with decreasing T . We are able to capture these effects because we treat Fe in heme as a Hund's impurity in the special electronic environment of oxy-heme by applying DFT+QMC. We think that the system is minimizing its energy by redistributing the electrons and developing magnetic correlations. These lead us to the notion that the binding of O₂ to Fe in heme is related to magnetism and the $3d$ Coulomb interactions.

In Extended Data Fig. 2(c), we see that, as the peak in $\langle n_{3d} \rangle$ develops, the total $3d$ magnetic

moment M_{3d} gets suppressed at the Fermi level. At low T , M_{3d} approaches $1.65 \mu_B$, which is close to the spin-1/2 value.

The electrons transferred to the Fe(3d) orbitals come mostly from a host state which we label as the $m = 171$ 'th host state. This state consists of the atomic orbitals from O₂ and the proximal histidine. Its wave function is illustrated in Extended Data Fig. 2(d). The electron occupation $\langle n_m \rangle$ of this state gets suppressed near the Fermi level at low temperatures, while its magnetic moment M_m gets enhanced reaching $0.6 \mu_B$ at 150 K as shown in Extended Data Figs. 2(e) and (f), respectively. In Extended Data Table I(c), we saw that the total host moment $M_h \approx 1.5 \mu_B$ at $T = 150$ K. Hence, as seen in Fig. 2(b), the total spin $S = 0$ state develops because of the antiferromagnetic correlations between basically a spin-1/2 localized at the Fe site and another spin-1/2 spread out at the neighboring O₂ and N sites.

It is important to note that the $S = 0$ spin state is possible because the electronic structure of oxy-heme is such that μ_F is located close to the upper-Hubbard level of the Fe($3d_{xy}$) orbital. When the Fermi level is away from the upper-Hubbard level of the $3d_{xy}$ orbital, we do not observe the charge transfer from O₂ to Fe and the magnetic gap. We also note that as the magnetic gap opens, basically no changes occur in the electron occupation numbers and the magnetic moments at the nitrogen sites which are nearest-neighbor to Fe. The magnetic moments at these nitrogen sites have already formed at higher temperatures.

The O₂ to Fe charge transfer and the opening of the spin gap are interesting electronic properties of oxy-heme. This is actually reminiscent of the Kondo effect where a localized magnetic moment in a metallic host gets completely screened by the formation of an antiferromagnetic screening cloud. In that case, the metallic host develops a magnetic moment by bringing in an electron from the boundary of the system at infinity. However, in the oxy-heme cluster, the host develops part of the screening moment by transferring electrons from the O₂ to the Fe(3d) orbitals.

Shift of the Fermi level with the temperature in oxy-heme

In Extended Data Fig. 3, we show results on the total electron number $\langle n_t \rangle$ versus μ for the oxy-heme cluster, which has 77 atoms and 350 electrons. We see that at 300 K the Fermi level $\mu_F \approx -3.8$ eV, while at $T = 150$ K we have $\mu_F \approx -3.9$ eV.

QMC finite- $\Delta\tau$ effects in the oxy-heme case

The Matsubara-time step $\Delta\tau$ is introduced in the QMC method by dividing the inverse temperature $\beta = 1/T$ into L Matsubara-time slices, $\beta = L\Delta\tau$. The QMC results become exact in the limit $\Delta\tau \rightarrow 0$. All of the DFT+QMC results shown in the above figures were taken by using $\Delta\tau$ values

between 0.125 and 0.2 eV⁻¹. In Extended Data Figures 4(a)-(d) we show the effects of using finite $\Delta\tau$ on $\langle n_t \rangle$, $\langle n_{3d} \rangle$, χ_t and M_t , respectively.

The charge-neutral oxy-heme cluster has 350 electrons. Extended Data Fig. 4(a) shows that $\langle n_t \rangle$ approaches 350.0 in the limit $\Delta\tau \rightarrow 0$ at $T = 150$ K. This result was obtained by using $\mu = -3.89$ eV. Hence, in the limit $\Delta\tau \rightarrow 0$ and at $T = 150$ K we have $\mu_F \approx -3.9$ eV. For 200 K, $\mu = -3.89$ eV was also used, while at $T = 300$ K we used $\mu = -3.8$ eV. These show that μ_F shifts from ≈ -3.8 eV at 300 K to ≈ -3.9 eV at 150 K with the opening of the spin gap.

In Extended Data Fig. 4(b), we see that, in the limit $\Delta\tau \rightarrow 0$, $\langle n_{3d} \rangle$ increases from 5.9 to approximately 6.1 as T decreases from 300 K to 150 K. Hence, Fe in oxy-heme is in a ferrous state.

Extended Data Fig. 4(c) shows that $\chi_t \rightarrow 150\mu_B^2$ as $\Delta\tau \rightarrow 0$ at 300 K, while for 200 K we see that χ_t extrapolates to a much reduced value. Hence, the magnetic gap is already developed at 200 K. When the $\Delta\tau \rightarrow 0$ corrections are taken into account, the drop in χ_t for $T < 300$ K, which was seen in Fig. 3(a), becomes more rapid. Similarly, in Extended Data Fig. 4(d) we observe a rapid drop in M_t in the limit $\Delta\tau \rightarrow 0$ as T decreases. These figures show that the finite- $\Delta\tau$ effects do not change our conclusions.

Calculation of the MCD spectrum in the UV region for deoxy-heme

Extended Data Fig. 5(a) illustrates the initial, intermediate and the final states in the $\pi \rightarrow \pi_1^*$ optical transition with LCP light absorption when the applied field is in the up direction. The left panel shows the initial state where the Fe($3d_v$) orbital, which is hybridizing with the bonding π state, has a down-spin electron, while the π state is doubly occupied. Because of the Fe($3d$)- π^* antiferromagnetic correlations, the antibonding π_1^* state has an up-spin electron. In the intermediate state (middle panel), we see that, upon LCP light absorption, the down-spin π electron moves to the π_1^* state, while the up-spin π electron spin-flips together with the Fe($3d$) down-spin electron through antiferromagnetic exchange. In this intermediate state, the up-spin Fe($3d$) electron is in an excited state because of the ferromagnetic Hund's coupling to the other Fe($3d$) spins. Hence, it spin-flips one more time by making use of the spin-orbit coupling at the Fe site, which leads to the final state (right panel). There is a similar process for the $\pi \rightarrow \pi_2^*$ transition with the RCP light absorption. These optical transitions are orbital selective because of the antiferromagnetic Fe- π^* correlations, which leads to the anomalous MCD line shape.

From comparisons with the optical absorption data, which will be shown below in Extended Data Fig. 7, we deduce that a bonding π state located at -5.6 eV, which we label as π_1 , is dominant

in the UV optical processes. In fact, we find that the leading contribution to UV MCD arises from the $\pi_1 \rightarrow \pi_1^*$ transition for the LCP light absorption, and $\pi_1 \rightarrow \pi_2^*$ for RCP absorption. Extended Data Figs. 5(b)-(d) show the wave functions of these π_1 , π_1^* , and π_2^* states, which consist of the $C(2p_z)$ atomic orbitals of the porphyrin layer.

Even though the π states do not have significant spin-orbit coupling, they can gain an effective coupling because of antiferromagnetic correlations and hybridization with the Fe(3d) orbitals. Extended Data Figs. 5(e)-(f) illustrate the lowest-order process where a π state can gain an effective spin-orbit coupling. We note that the largest hybridization matrix elements of the π_1^* and π_2^* states are with the $3d_{xz}$ and $3d_{yz}$ orbitals, respectively, and they are both about 0.3 eV.

We use the following simple expression for the T -dependent MCD spectrum in the UV region

$$\Delta I(E) = \sum_m \left(C_1 |\langle \pi_1^* | \mathbf{p} | m \rangle|^2 A_{\pi_1^*}(\epsilon_m + E) - C_2 |\langle \pi_2^* | \mathbf{p} | m \rangle|^2 A_{\pi_2^*}(\epsilon_m + E) \right) f(\epsilon_m)(1 - f(\epsilon_m + E)), \quad (3)$$

which is due to LCP $\pi \rightarrow \pi_1^*$ and RCP $\pi \rightarrow \pi_2^*$ optical transitions. Here, m sums over all of the bonding π host states, and C_1 and C_2 are coefficients to be determined. In addition, we use the matrix element $|\langle m' | \mathbf{p} | m \rangle|^2$, instead of $|\langle m' | p_- | m \rangle|^2$ or $|\langle m' | p_+ | m \rangle|^2$ where $p_{\pm} = p_x \pm ip_y$, since the experiments were performed using samples in solution.

In Extended Data Fig. 6(a)-(d), we show QMC data on the electronic properties of the π_1^* and π_2^* host states. Their spectral weights $A(\omega)$ are obtained in an approximate way by taking the derivative with respect to μ of their electron occupations $\langle n \rangle$ shown in Extended Data Fig. 6(a). The resulting $A_{\pi_1^*}(\omega)$ and $A_{\pi_2^*}(\omega)$ are shown in Extended Data Fig. 6(b). These spectral weights have peaks split by 0.2 eV corresponding to $2J_{AF}$, where $J_{AF} \sim 4|V_{\pi^*,v}|^2/U \sim 0.1$ eV is the maximum value of the Fe(3d_v)- π^* antiferromagnetic exchange constant. Extended Data Fig. 6(c) shows $\langle (M^z)^2 \rangle$ versus μ for π_1^* and π_2^* . Extended Data Fig. 6(d) shows the function $\langle M_{3d}^z M_m^z \rangle$ between Fe(3d) and the $m = \pi_1^*$ and π_2^* states. Here, we clearly see the Fe(3d)- π^* antiferromagnetic correlations.

In Eq. (3) we take the ratio C_1/C_2 to be 4. This is the only fitting parameter we use in obtaining the spectrum shown in Fig. 4(e). Since π_1^* is already occupied by one up-spin electron and π_2^* is nearly empty, we expect the coefficient C_1 to be larger than C_2 . Finally, since the polarizability of the total Fe(3d) spin has $1/T$ temperature dependence, our result for the MCD intensity also exhibits this type T -dependence.

Comparison of the MCD and the optical absorption data in the UV region for deoxy heme

Extended Data Fig. 7(a) shows experimental data on the optical absorption of deoxy-heme⁴. The peak near 3 eV originates from $\pi \rightarrow \pi^*$ transitions. This peak has an asymmetrical line shape, where the intensity below 2.8 eV is much reduced compared to the high energy tail.

A simple estimate of the optical absorption in the UV region is given by

$$I(E) = \sum_{m',m} |\langle m' | \mathbf{p} | m \rangle|^2 f(\epsilon_m)(1 - f(\epsilon_{m'})) \delta(E - (\epsilon_{m'} - \epsilon_m)), \quad (4)$$

where m and m' sum over the bonding π and antibonding π^* host states, respectively, and $\mathbf{p} = \sum_i (-e)\mathbf{r}_i$ is the operator for the electric-dipole moment of the cluster. Here, for ϵ_m we have used the DFT results, since the Coulomb interactions taken into account by QMC do not produce a significant shift in the doubly-occupied π states. The results for $I(E)/E$ are shown as the black bars for each transition in Extended Data Fig. 7(b). The solid curve was obtained by using a broadening of 0.1 eV for the δ -functions. Comparison with the experimental data shows that the dominant contribution to optical absorption is coming from the $\pi_1 \rightarrow \pi_1^*$ and $\pi_1 \rightarrow \pi_2^*$ transitions, where π_1 is located at -5.6 eV. We calculated the MCD spectra allowing only for these two transitions. The result is the black curve shown in Extended Data Fig. 8, which is in better agreement with the experimental data of Fig. 4(d).

Extended Data Fig. 6(b) shows that the spectral-weight functions of the π_1^* and π_2^* states overlap in energy by about 0.2 eV. We artificially eliminated this overlap by shifting the spectral weight of the π_2^* state by 0.2 eV higher in energy. Its result is shown as the red dashed curve in Extended Data Fig. 8. Hence, we obtain the best agreement with the experimental MCD data when π_1^* and π_2^* spectral weights have no overlap.

Extended Data Table I | Additional DFT+QMC data on the charge and spin distributions, and the magnetic correlations

$\langle n_v \rangle$	xy	xz	yz	$3z^2 - r^2$	$x^2 - y^2$	total ($\langle n_d \rangle$)
deoxy (300 K)	1.00	1.12	1.06	1.07	1.13	5.38
oxy (300 K)	1.84	1.17	1.15	0.92	0.75	5.83
oxy (150 K)	1.88	1.32	1.34	0.85	0.68	6.07

(a) Electron occupation number $\langle n_v \rangle$ of the Fe($3d_v$) orbitals.

$M_v^{\text{eff}} (\mu_B)$	xy	xz	yz	$3z^2 - r^2$	$x^2 - y^2$
deoxy (300 K)	0.99	0.93	0.96	0.95	0.93
oxy (300 K)	0.40	0.89	0.89	0.79	0.74
oxy (150 K)	0.35	0.77	0.76	0.77	0.72

(b) Effective magnetic moment M_v^{eff} of the Fe($3d_v$) orbitals.

	M_{3d}	M_h	$\langle M_{3d}^z M_h^z \rangle$	M_t	S_{3d}	S_h	S
deoxy (300 K)	4.56	1.06	-2.65	4.07	1.83	0.23	1.60
oxy (300 K)	2.50	1.32	-1.71	2.13	0.85	0.33	0.68
oxy (150 K)	1.65	1.50	-2.30	0.61	0.47	0.40	0.10

(c) Effective magnetic moments and effective spins. Here, M_{3d} , M_h and M_t denote the Fe($3d$), host and the total effective magnetic moments (in units of μ_B), respectively, while $\langle M_{3d}^z M_h^z \rangle$ is the Fe($3d$)-host magnetic correlation function (in μ_B^2). In addition, S_{3d} , S_h and S denote the Fe($3d$), host and the total effective spins, respectively.

$\langle M_V^z M_{V'}^z \rangle$	xy	xz	yz	$3z^2 - r^2$	$x^2 - y^2$
xy	0.98	0.84	0.90	0.88	0.84
xz		0.86	0.79	0.77	0.73
yz			0.92	0.83	0.78
$3z^2 - r^2$				0.90	0.77
$x^2 - y^2$					0.86

(d) Magnetic correlation function $\langle M_V^z M_{V'}^z \rangle$ among the $Fe(3d_V)$ orbitals for the deoxy-heme cluster at $T = 300$ K.

$\langle M_V^z M_{V'}^z \rangle$	xy	xz	yz	$3z^2 - r^2$	$x^2 - y^2$
xy	0.16	0.06	0.06	0.04	0.01
xz		0.79	0.60	0.25	0.14
yz			0.81	0.25	0.14
$3z^2 - r^2$				0.62	0.08
$x^2 - y^2$					0.55

(e) Magnetic correlation function $\langle M_V^z M_{V'}^z \rangle$ among the $Fe(3d_V)$ orbitals for the oxy-heme cluster at $T = 300$ K.

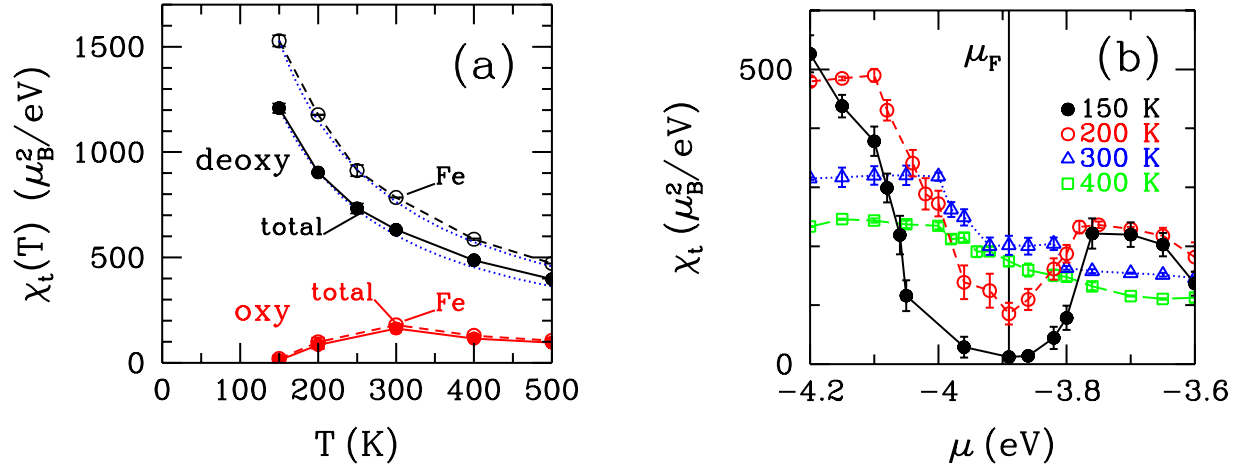
$\langle M_V^z M_{V'}^z \rangle$	xy	xz	yz	$3z^2 - r^2$	$x^2 - y^2$
xy	0.12	0.02	0.02	0.02	0.00
xz		0.59	-0.09	0.05	0.04
yz			0.58	0.04	0.04
$3z^2 - r^2$				0.59	0.04
$x^2 - y^2$					0.52

(f) Magnetic correlation function $\langle M_V^z M_{V'}^z \rangle$ among the $Fe(3d_V)$ orbitals for the oxy-heme cluster at $T = 150$ K.

	$\sum_v \langle (M_v^z)^2 \rangle$	$\sum_{v \neq v'} \langle M_v^z M_{v'}^z \rangle$	$\langle (M_{3d}^z)^2 \rangle$
deoxy (300 K)	4.5	16.2	20.7
oxy (300 K)	2.9	3.3	6.2
oxy (150 K)	2.4	0.3	2.7

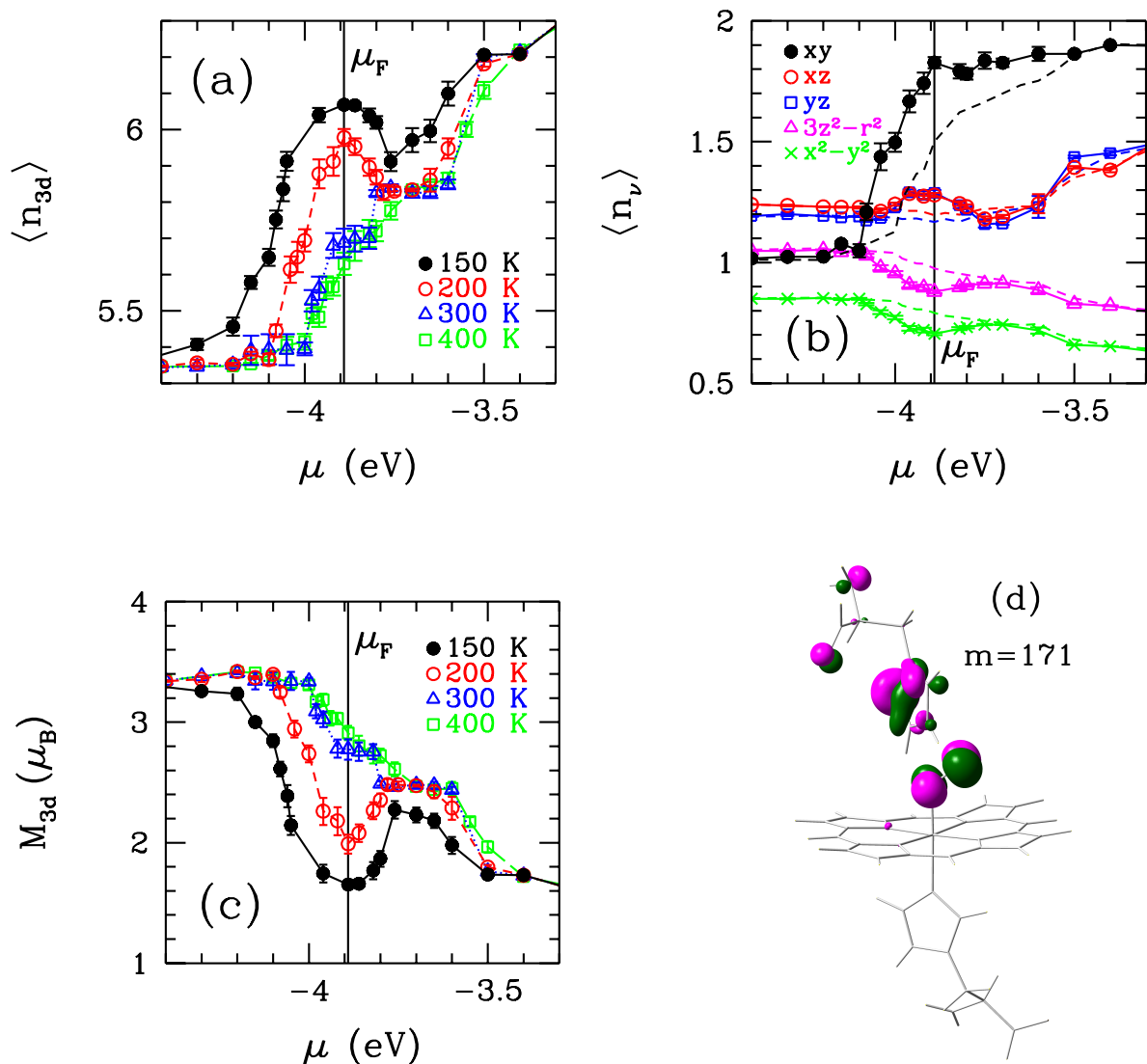
(g) Comparison of the intra and inter-orbital Fe(3d) magnetic correlations (in units of μ_B^2) contributing to $(M_{3d})^2$, the square of the effective total Fe(3d) moment.

Extended Data Fig. 1 | Additional DFT+QMC results on the spin susceptibility

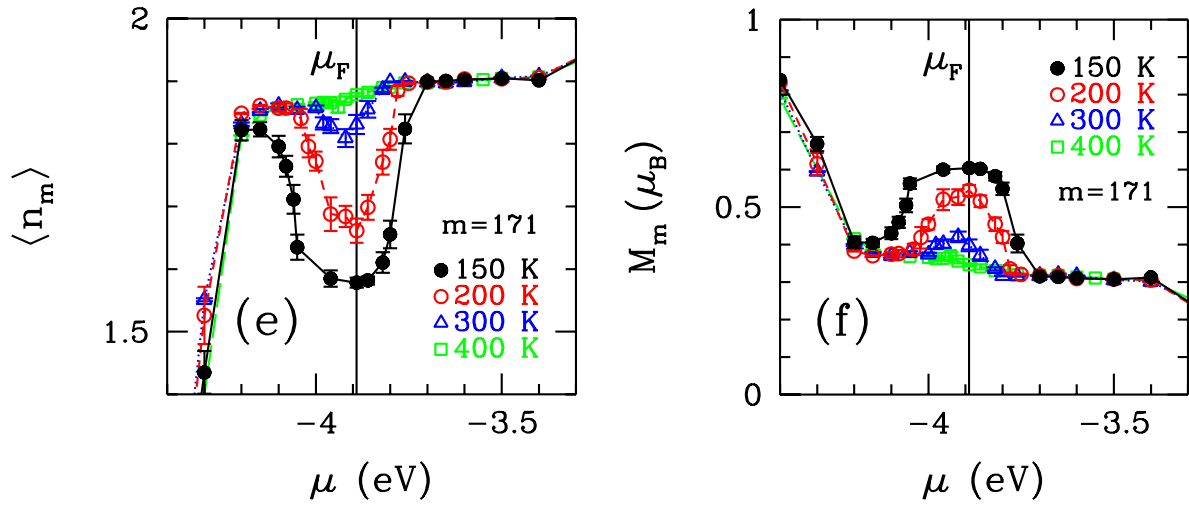


(a) Total spin susceptibility χ_t of the deoxy and oxy-heme clusters denoted by the filled circles plotted as a function of the temperature. The results on the Fe spin susceptibility χ_{Fe} denoted by the open circles are also shown. Here, the blue dotted lines denote the $1/T$ temperature dependence. (b) χ_t versus the chemical potential μ near the Fermi level μ_F at various temperatures. Here, the black vertical line denotes μ_F at $T = 150$ K.

Extended Data Fig. 2 | Additional DFT+QMC data on the charge transfer from O₂ to Fe in oxy-heme

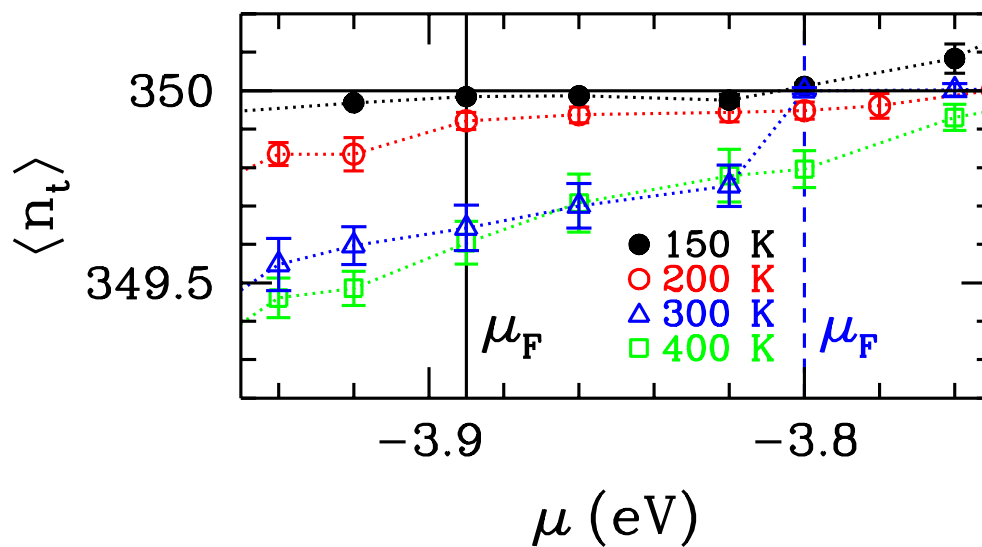


(a) Total number of the electrons in the Fe(3d) orbitals $\langle n_{3d} \rangle$ plotted as a function of the chemical potential μ at various temperatures. (b) Electron occupation number of the Fe(3d_v) orbitals $\langle n_v \rangle$ versus μ . Here, the data points connected by the solid lines denote $\langle n_v \rangle$ obtained at 200 K, while the dashed curves denote results obtained at 400 K. (c) Total magnetic moment of the Fe(3d) orbitals M_{3d} versus μ . (d) Illustration of the wave function of the $m = 171$ 'th host state, which is real valued. Here, the magenta and green colors denote the positive and the negative regions.



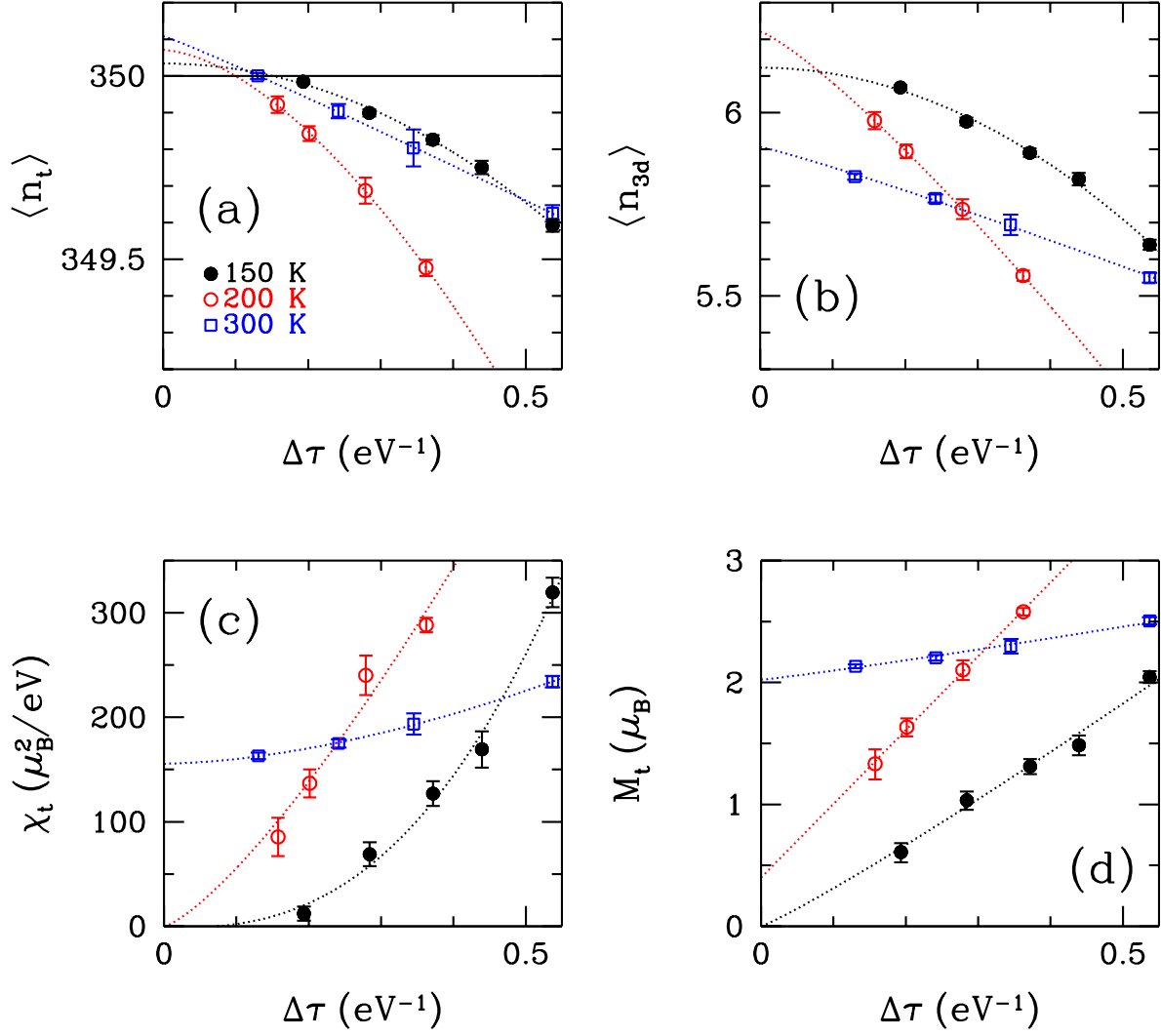
(e) Electron number of the $m = 171$ 'th host state $\langle n_m \rangle$ versus μ . (f) Magnetic moment of the $m = 171$ 'th host state M_m versus μ . In these figures, the black vertical line denotes the Fermi level μ_F at $T = 150$ K.

Extended Data Fig. 3 | Shift of the Fermi level with the temperature for oxy-heme



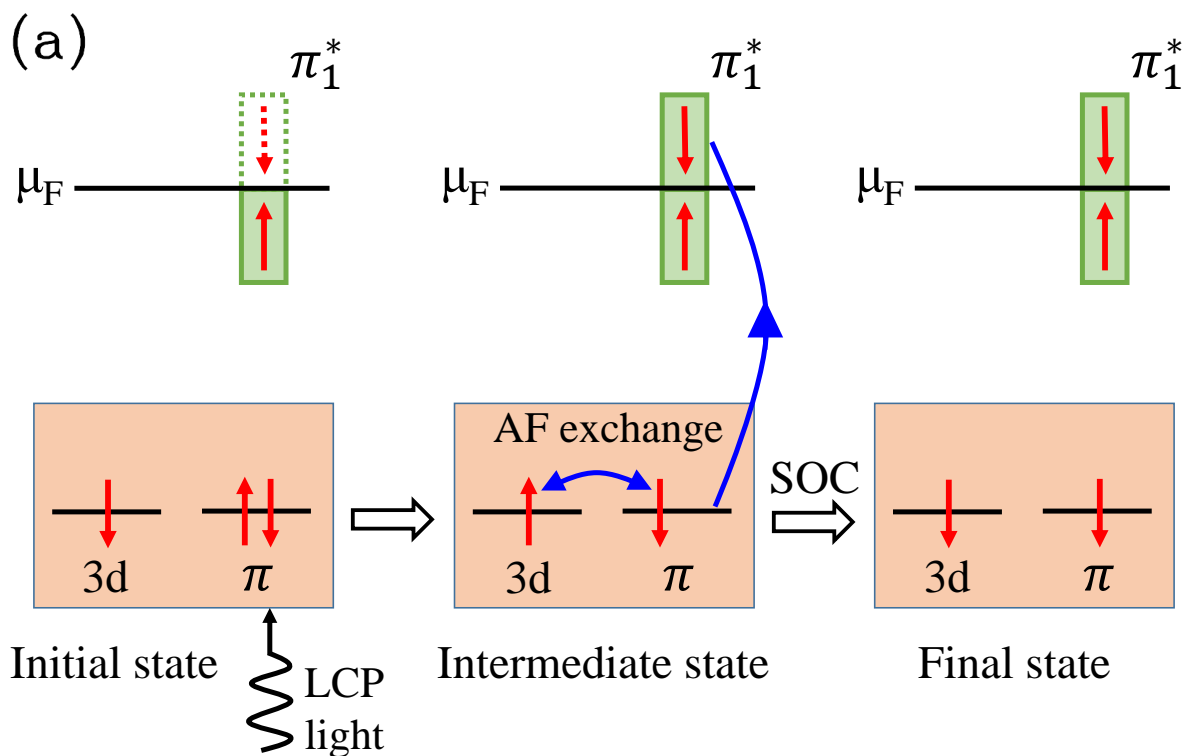
Total electron number of the oxy-heme cluster $\langle n_t \rangle$ versus the chemical potential μ at various temperatures. The charge-neutral oxy-heme cluster has 350 electrons. We see that, as the temperature is lowered, the Fermi level μ_F shifts from ≈ -3.8 eV at 300 K to ≈ -3.9 eV at 150 K.

Extended Data Fig. 4 | QMC finite- $\Delta\tau$ effects in the oxy-heme case

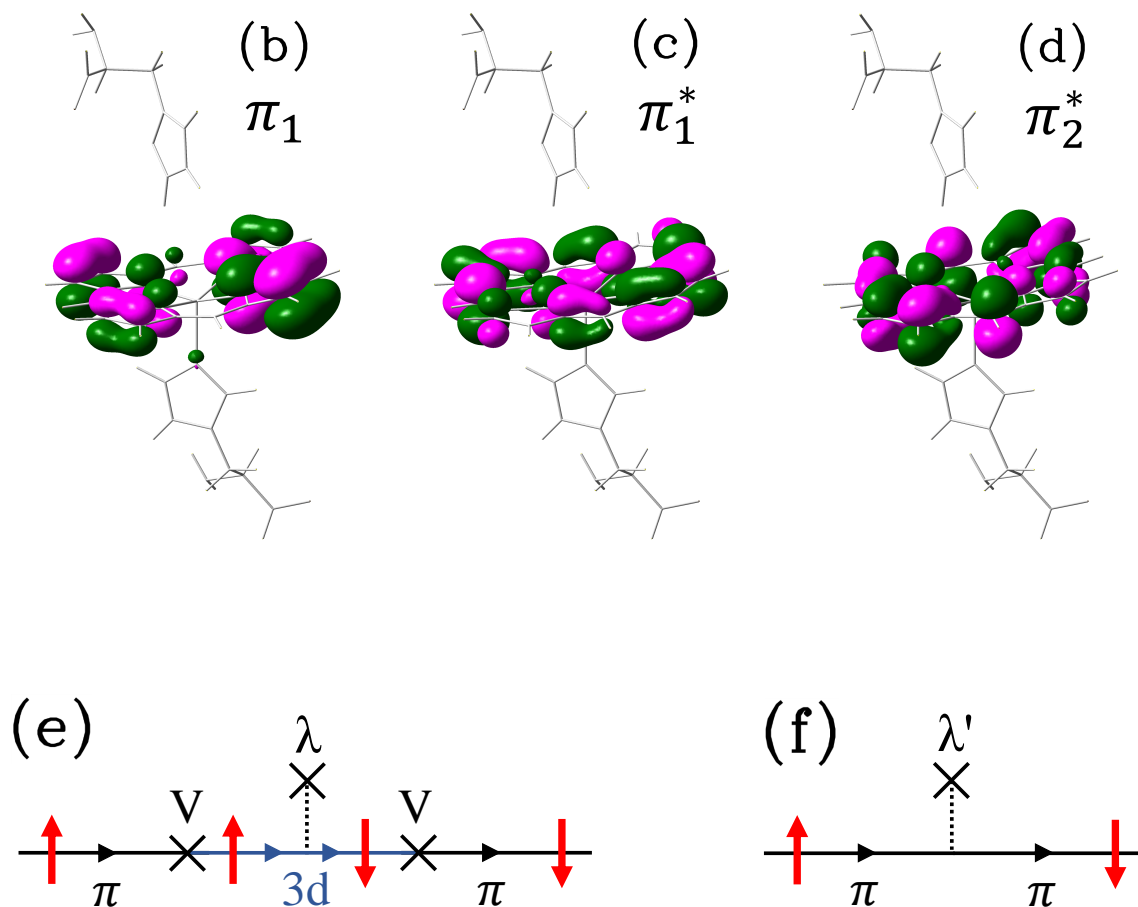


(a) Total number of the electrons in the cluster $\langle n_t \rangle$, (b) the total electron number in the Fe(3d) orbitals $\langle n_{3d} \rangle$, (c) the total spin susceptibility χ_t , and (d) the total magnetic moment M_t plotted as a function of $\Delta\tau$ for the various values of T shown in (a). Here, $\Delta\tau$ is the Matsubara-time step used in the QMC simulations. The dotted curves are the least-squares fits to the QMC data.

Extended Data Fig. 5 | Electronic transitions for the anomalous MCD spectrum of deoxy-heme

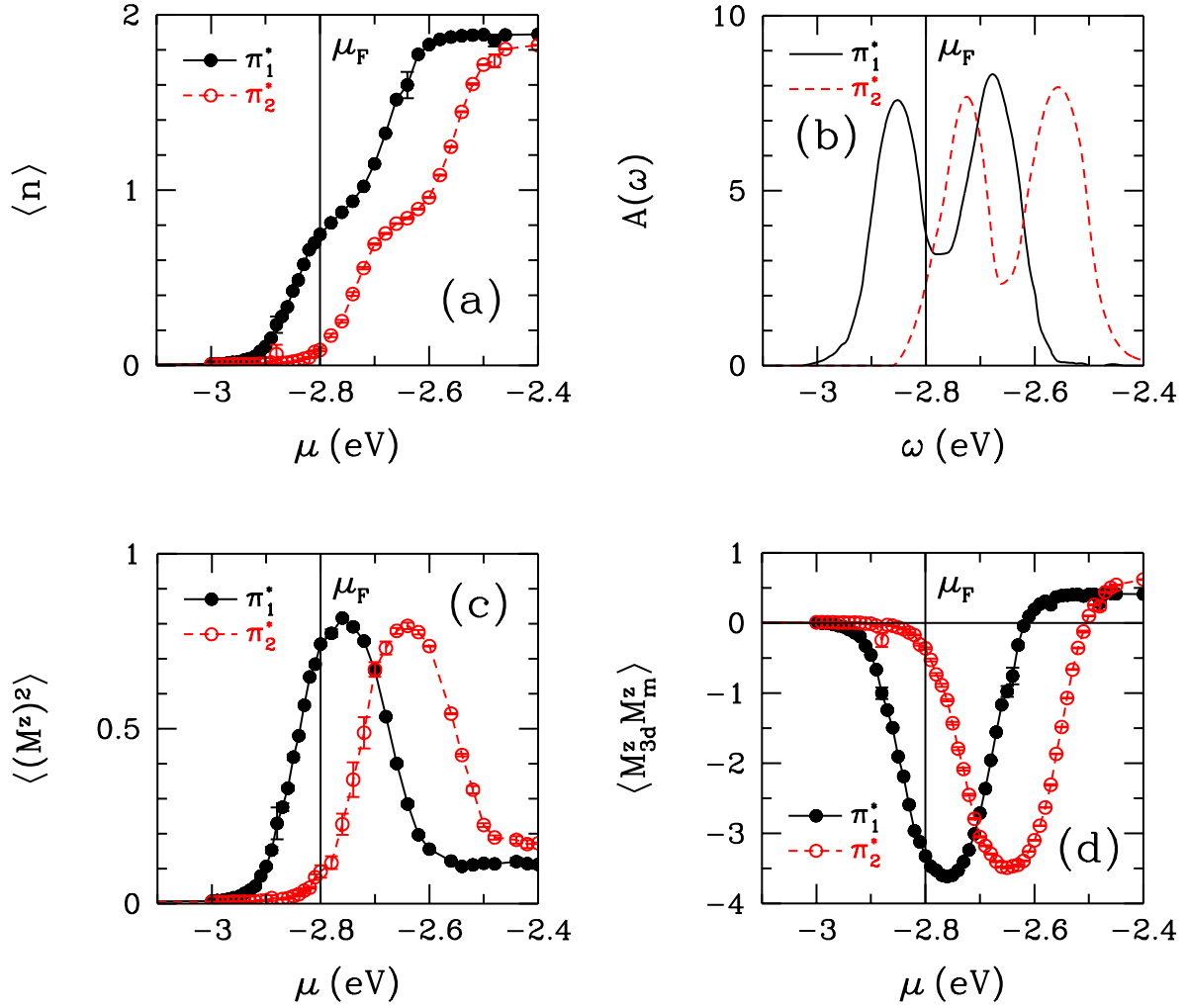


(a) Illustration of the initial, intermediate and the final states in the $\pi \rightarrow \pi_1^*$ transition with LCP light absorption in MCD in the UV region. These panels are for an applied magnetic field pointing in the up direction, which is also along the direction of light propagation.



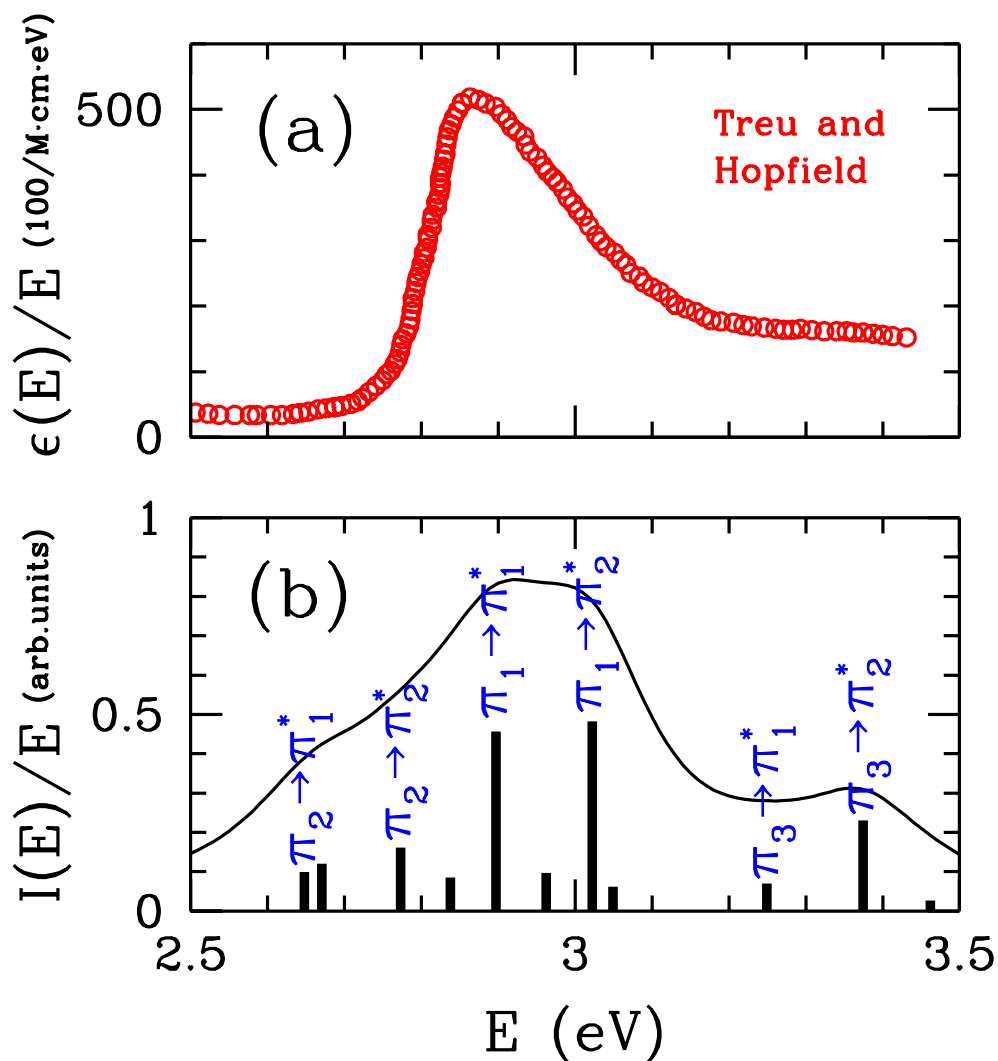
(b)-(d) Illustration of the wavefunctions for the bonding π_1 and the antibonding π_1^* and π_2^* host states, respectively. (e) Feynman diagram illustrating a hybridization process through which an electron in a bonding π state gains an effective spin-orbit coupling. Here, an up-spin electron in the π state can become an up-spin $3d$ electron through hybridization. Because of the spin-orbit coupling at the Fe site, this up-spin $3d$ electron can now flip its spin down. Through hybridization for a second time, it then becomes a down-spin π electron. This is the lowest-order diagram to the set of processes where the π state gains an effective spin-orbit coupling. Here, V is the hybridization matrix element between the π state and the Fe($3d$) orbitals, and λ is the spin-orbit coupling constant for the Fe($3d$) orbitals. (f) Because of processes as shown in (e), an electron in a π state can gain an effective spin-orbit coupling λ' .

Extended Data Fig. 6 | Electronic properties of the π_1^* and π_2^* host states located near the Fermi level in deoxy-heme



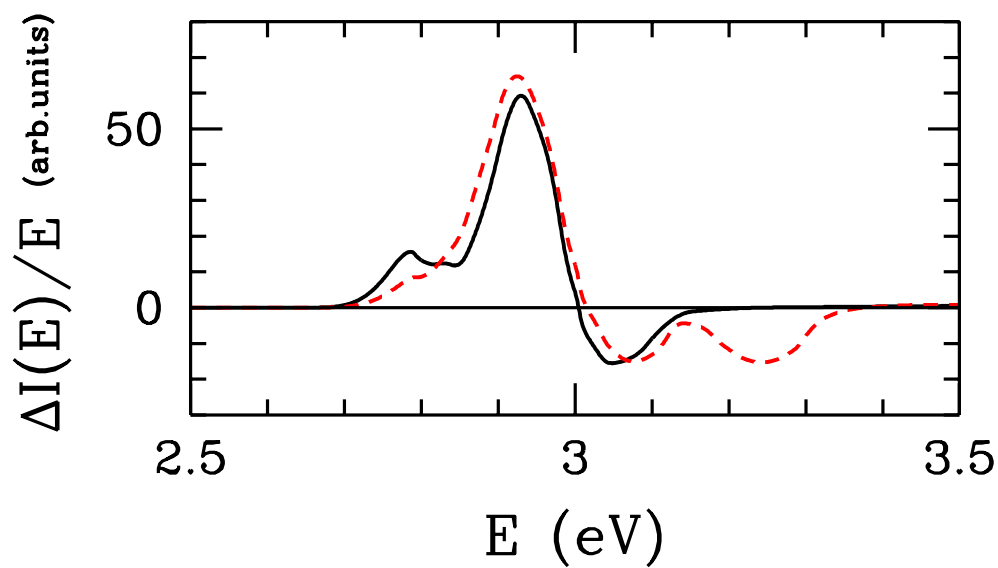
(a) Electron occupation $\langle n \rangle$ of the π_1^* and π_2^* host states plotted as a function of the chemical potential μ . (b) Single-particle spectral weight $A(\omega)$ versus ω for the π_1^* and π_2^* states obtained from the $\langle n \rangle$ versus μ results shown in (a). (c) Square of the magnetic moment of the π_1^* and π_2^* states versus μ . (d) Magnetization correlation function of the Fe(3d) magnetic moment with the moments of the π_1^* and π_2^* states $\langle M_{3d}^z M_m^z \rangle$ versus μ . In these figures, the black vertical line denotes the Fermi level μ_F , and the results are presented for $T = 300$ K.

Extended Data Fig. 7 | Experimental and calculated results on the optical absorption in UV region for deoxy-heme



(a) Experimental data on the frequency dependence of the optical absorption normalized by energy $\epsilon(E)/E$ for deoxy-HbA by Treu and Hopfield⁴. (b) Calculated optical absorption normalized by energy $I(E)/E$ for deoxy-heme. The black bars denote the weights of the various $\pi \rightarrow \pi^*$ transitions. Here, we have labelled the π states which give the leading contributions as π_1 , π_2 and π_3 . We have also indicated which particular $\pi \rightarrow \pi^*$ transitions the bars correspond to. The black curve was obtained by artificially broadening the delta functions by 0.1 eV.

Extended Data Fig. 8 | MCD spectrum due to $\pi_1 \rightarrow (\pi_1^*, \pi_2^*)$ optical transitions



Here, the black curve denotes the MCD spectrum for when only the $\pi_1 \rightarrow \pi_1^*$ and $\pi_1 \rightarrow \pi_2^*$ transitions are taken into account. The red-dashed curve denotes the same in the case where the π_2^* state is artificially shifted by 0.2 eV to higher energies so that there is no overlap with the π_1^* state. This yields the best agreement with the experimental line shape seen in Fig. 4(d).

SUPPLEMENTARY INFORMATION

Calculation of the Anderson model parameters with DFT for heme clusters

We obtain the one-electron parameters ε_m , $\varepsilon_{d\nu}$ and $V_{m\nu}$ of the effective Anderson model by making use of the DFT method. These calculations are performed for a reduced cluster with molecular coordinates obtained from the Protein Data Bank. In this calculation, instead of the atomic orbitals, we use the natural atomic orbitals (NAO's)¹, which form an orthonormal basis. First, we express the Fock matrix in the NAO basis. We take the Fe($3d_\nu$) NAO's as the impurity orbitals and their energy levels as $\varepsilon_{d\nu}$'s in the Anderson Hamiltonian. Diagonalizing the remaining part of the Fock matrix, we obtain the host eigenstates $|u_m\rangle$ and their energy levels ε_m and the hybridization matrix elements $V_{m\nu}$. This procedure is explained in more detail in Ref.^{2,3}. The DFT calculations are carried out by using the Gaussian program⁴ with the BP86 energy functional^{5,6} and the 6-31G basis set with 483 basis functions for the deoxy-heme cluster and 501 basis functions for the oxy-heme cluster. We use ε_m , $\varepsilon_{d\nu}$ and $V_{m\nu}$ determined this way as input parameters for the QMC simulations.

Truncated heme clusters and the finite-size effects

The deoxy-HbA molecule seen in Fig. 1(a) contains four inequivalent heme groups, $\alpha_1 - \alpha_2 - \beta_1 - \beta_2$. The nearest-neighbor Fe-Fe distance varies between 34 Å and 39.5 Å. Since this molecule consists of about 9700 atoms, we performed our calculations for a reduced heme cluster obtained from the α_1 group, which is shown in Fig. 1(b). This cluster contains the porphyrin ring with Fe at the center, located below porphyrin is the distal histidine with the imidazole part, and also located at the top is the proximal histidine. It is thought that the proximal histidine is necessary for the stability of O₂ binding⁷. In obtaining this truncated cluster, we have replaced the methyl, vinyl and propionate side groups of porphyrin with hydrogen atoms. We have determined the coordinates of these substituted hydrogens by DFT optimization. The deoxy-heme cluster obtained this way consists of 75 atoms and 334 electrons (C₃₂H₃₀FeN₁₀O₂). In order to obtain the oxy-heme cluster, we have again started with the molecular structure of oxy-HbA determined by X-ray measurements from the Protein Data Bank (Keyword: 2DN1). From the α_1 heme group we have obtained the cluster seen in Fig. 1(c) with 77 atoms and 350 electrons (C₃₂H₃₀FeN₁₀O₄).

In obtaining the energy spectrum of the cluster with DFT, it is necessary to take into account the finite size effects arising from the boundary of the cluster. Even though the HbA molecule contains about 9700 atoms, we retain only 75 atoms for the deoxy-heme cluster shown in Fig.

1(b). In this case we find that a host state which is localized on the oxygen and carbon sites at the boundary of the cluster (at the lower edge of the cluster shown in Fig. 1(b)) has an energy close to the Fermi level. However, when we use larger clusters containing 87 or 96 atoms so that the distal histidine part contains more sites and the oxygen site is not close to the boundary, we find that this host state arising from the boundary moves away from the Fermi level to higher energies. Hence, for the 75 site cluster we have by hand removed the boundary host state in order to control the finite size effects.

QMC measurements

In the DFT+QMC approach, the Coulomb interactions at the $\text{Fe}(3d_\nu)$ orbitals are taken into account by both the DFT and the QMC techniques. In order to prevent this double counting, an orbital-dependent double-counting term μ_ν^{DC} defined as

$$\mu_\nu^{\text{DC}} = \frac{1}{2}U n_{d\nu}^0 + \frac{1}{2}(U' + U'') \sum_{\nu' \neq \nu} n_{d\nu'}^0 \quad (5)$$

is subtracted from the bare $\text{Fe}(3d_\nu)$ energy levels, $\epsilon_{d\nu} \rightarrow \epsilon_{d\nu} - \mu_\nu^{\text{DC}}$. Here, $n_{d\nu}^0$ is the electron number in the $\text{Fe}(3d_\nu)$ NAO's obtained by the DFT calculations.

By using QMC simulations we calculate the expectation values of various operators to study the electronic properties of the effective Anderson model for heme. In particular, we calculate the distribution of the magnetic moments in the cluster, the correlations among these moments, the magnetic susceptibilities and in addition the charge distribution throughout the cluster. The electron occupation number of the $\text{Fe}(3d_\nu)$ orbitals is obtained from

$$\langle n_\nu \rangle = \sum_{\sigma} \langle d_{\nu\sigma}^\dagger d_{\nu\sigma} \rangle, \quad (6)$$

where the expectation value of an operator A is defined by

$$\langle A \rangle = \frac{1}{Z} \text{Tr} e^{-\beta H} A \quad (7)$$

with $Z = \text{Tr} e^{-\beta H}$ the partition function. In addition, we calculate the effective magnetic moments M_ν^{eff} of the $\text{Fe}(3d_\nu)$ orbitals from

$$M_\nu^{\text{eff}} = \sqrt{\langle (M_\nu^z)^2 \rangle}, \quad (8)$$

where the longitudinal magnetization operator for the $\text{Fe}(3d_\nu)$ orbital is defined in units of μ_B as

$$M_\nu^z = d_{\nu\uparrow}^\dagger d_{\nu\uparrow} - d_{\nu\downarrow}^\dagger d_{\nu\downarrow}. \quad (9)$$

We calculate the total Fe(3d) spin susceptibility from

$$\chi_{3d} = \int_0^\beta d\tau \langle M_{3d}^z(\tau) M_{3d}^z(0) \rangle \quad (10)$$

where the total Fe(3d) magnetization operator is $M_{3d}^z = \sum_v M_v^z$ with the Matsubara-time evolution $M_{3d}^z(\tau) = \exp(H\tau) M_{3d}^z \exp(-H\tau)$. Similarly, the total spin susceptibility of the cluster is obtained from

$$\chi_t = \int_0^\beta d\tau \langle M_t^z(\tau) M_t^z(0) \rangle \quad (11)$$

where the total magnetization operator of the cluster is $M_t^z = M_{3d}^z + M_h^z$ and the total magnetization operator of the host is $M_h^z = \sum_m M_m^z$ with

$$M_m^z = c_{m\uparrow}^\dagger c_{m\uparrow} - c_{m\downarrow}^\dagger c_{m\downarrow} \quad (12)$$

in units of μ_B . In evaluating the integrand in Eq. (7), we include the correlations among the Fe(3d_v) orbitals, and the Fe(3d)-host correlations in addition to the intra-orbital host correlations as seen in

$$\langle M_t^z(\tau) M_t^z(0) \rangle = \sum_{v,v'} \langle M_v^z(\tau) M_{v'}^z(0) \rangle + 2 \sum_{v,m} \langle M_v^z(\tau) M_m^z(0) \rangle + \sum_m \langle M_m^z(\tau) M_m^z(0) \rangle. \quad (13)$$

However, we do not include the contribution coming from the inter-orbital host correlations

$$\sum_{m,m' \neq m} \langle M_m^z(\tau) M_{m'}^z(0) \rangle, \quad (14)$$

because its effect on χ_t is negligible compared to the other terms. In the oxy-heme case, we estimate its contribution to χ_t to be less than $\approx 4\mu_B^2/\text{eV}$.

Calculation of the magnetic-moment density

Here, we describe how we calculate the magnetic-moment density $M(\mathbf{r})$ for the heme clusters. The effective magnetic moment of the m 'th host state is obtained from

$$M_m^{\text{eff}} = \sqrt{\langle (M_m^z)^2 \rangle}. \quad (15)$$

While constructing the effective Anderson Hamiltonian for the heme cluster from the Fock matrix, we have obtained the expansion of the host states in terms of the atomic orbitals,

$$c_{m\sigma} = \sum_i D_{m,i} \tilde{c}_{i\sigma}, \quad (16)$$

where $\tilde{c}_{i\sigma}$ destroys an electron with spin σ in the i 'th atomic orbital. Hence, the magnetization operator of the m 'th host state can be written as

$$M_m^z = \sum_{i,j} D_{m,i}^* D_{m,j} (\tilde{c}_{i\uparrow}^\dagger \tilde{c}_{j\uparrow} - \tilde{c}_{i\downarrow}^\dagger \tilde{c}_{j\downarrow}). \quad (17)$$

In order to obtain a simple illustration of the magnetization density, we neglect the correlations for when $i \neq j$, and define the following approximate expression as the magnetic-moment density for the host states

$$M(\mathbf{r}) \approx \sum_{m,i} M_m^{\text{eff}} |D_{m,i}|^2 \delta(\mathbf{r} - \mathbf{r}_i), \quad (18)$$

where \mathbf{r}_i is the coordinate of the i 'th atomic orbital. Using this expression, we show in Fig. 2 the Fe(3d) and the host magnetic-moment density in the basis of the atomic orbitals as a bubble graph. We use the sign of the Fe(3d)-host correlation function $\langle M_{3d}^z M_m^z \rangle$ to determine the sign of $M(\mathbf{r})$. In obtaining $M(\mathbf{r})$ from Eq. (14), we have only included the contributions from host states with $|M_m^{\text{eff}}| > 0.1 \mu_B$, since it is difficult to obtain M_m^{eff} accurately for when $\langle (M_m^z)^2 \rangle < 0.01 \mu_B^2$. Hence, Fig. 2 does not show the long-range tail of the magnetic-moment density away from the Fe site. It is cut-off when $|M(\mathbf{r})| \lesssim 0.1 \mu_B$.

* nejatbulut@iyte.edu.tr

- ¹ Reed, A. E., Curtiss, L. A. & Weinhold, F. Intermolecular interactions from a natural bond orbital, donor-acceptor viewpoint. *Chem. Rev.* **88**, 899 (1988).
- ² Kandemir, Z., Mayda, S. & Bulut, N. Electronic structure and correlations of vitamin B₁₂ studied within the Haldane-Anderson impurity model. *Eur. Phys. J. B* **89**, 113 (2016).
- ³ Mayda, S., Kandemir, Z. & Bulut, N. Electronic structure of cyanocobalamin: DFT+QMC study. *J. Supercond. Nov. Magn.*, **30**, 3301 (2017).
- ⁴ Frisch, M. J. et al. : Gaussian 09, Revision D.01. Gaussian, Inc., Wallingford, CT (2009).
- ⁵ Becke, A. D. Density-functional exchange-energy approximation with correct asymptotic behavior. *Phys. Rev. A* **38**, 3098 (1988).
- ⁶ Perdew, J. P. Density-functional approximation for the correlation energy of the inhomogeneous electron gas. *Phys. Rev. B* **33**, 8822 (1986).
- ⁷ Birukou, I., Schweers, R. L. & Olson, J. S. Distal histidine stabilizes bound O₂ and acts as a gate for ligand entry in both subunits of adult human hemoglobin. *J. Bio. Chem.* **285**, 8840 (2010).